SHM
Structural Health Monitoring

Embedded-ultrasonics Structural Radar for *In Situ* Structural Health Monitoring of Thin-wall Structures

Victor Giurgiutiu[1,*] and JingJing Bao[2]

[1]*Mechanical Engineering Department, University of South Carolina, Columbia, SC 29208, USA*
[2]*Racer Technology Ltd. Co., Beijing, China 100053*

Embedded-ultrasonics structural radar (EUSR) is a new concept and methodology for *in situ* nondestructive evaluation (NDE) and structural health monitoring (SHM) of thin-wall structures. EUSR consists of: (a) an array of piezoelectric wafer active sensors (PWAS) embedded into the structure; and (b) electronic modules for signal transmission/reception, processing, and interpretation. EUSR utilizes guided elastic waves (Lamb waves) generated omnidirectionally into the thin-wall structure by surface-mounted permanently attached PWAS. The paper starts with the general concepts of the EUSR algorithm: transmission beamforming, reception beamforming, and time-of-fight (TOF) determination. Next, details of the Lamb wave generation with PWAS, verification of group-velocity dispersion curves, identification of optimal excitation frequency, and confirmation of wave front omnidirectionality are discussed. In the third part of the paper, the actual implementation of the EUSR method in a proof-of-concept demonstration is presented. The construction of the PWAS-phased array is described, and detection of cracks located broadside and offside of the PWAS array is illustrated. The method is shown to be easy to use through a visually interactive LabView[TM] interface. Very good detection accuracy is observed. The proof-of-concept experiments presented in this paper were illustrated on metallic structures; however, the EUSR concept may also work on composite and hybrid structures, although the range of detection may be reduced by the medium attenuation.

Keywords   *in situ* diagnostics · phased array · structural health monitoring · ultrasonic · Lamb wave · piezoelectrics · PWAS · NDE

1   Introduction

The advantages of using a phased array of transducers for ultrasonic testing are multiple [1,2]. The Krautkramer company [3] produces a line of phased-array transducers for the inspection of very thick specimens, and for the sidewise inspection of thick slabs, etc. (Figure 1a). The principles of phased-array ultrasonic inspection resemble the phased-array principles used in radar, sonar, seismology, oceanography, and medical imaging [4]. The common terminology between these application fields, such as the term "phased array", shows their common ancestry.

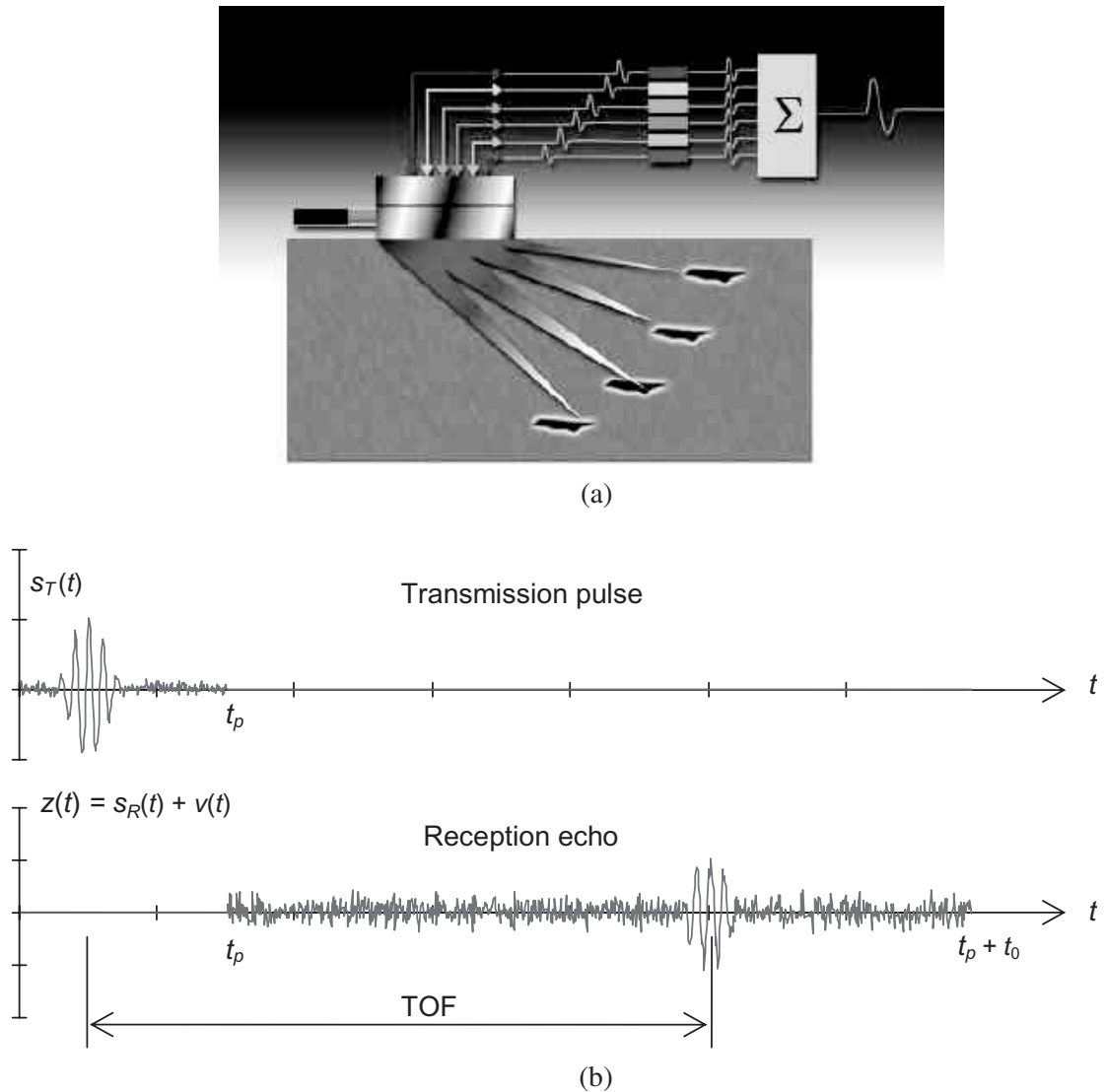*Author to whom correspondence should be addressed.
E-mail: victorg@sc.edu

(a)

(b)

Figure 1   (a) Conceptual representation of phased-array principles [3]; (b) the pulse-echo method.

Phased arrays are made up of N elements, usually identical in size, which are arranged along a line at uniform pitch. The wave pattern generated by the phased array is the result of the superposition of the waves generated by each individual element. By sequentially firing the individual elements of an array transducer at slightly different times, the ultrasonic wavefront can be focused or steered in a specific direction [5]. Thus, inspection of a wide zone can be achieved by electronically sweeping and/or refocusing without physically manipulating the transducer.

Once the beam steering and focusing have been established, the detection of internal flaws is done with the pulse-echo method (Figure 1b). A pulse, consisting of a smooth-windowed tone-burst of duration t_p, is transmitted toward the target. The target reflects the signal and creates an echo, which is detected by the sensor. By analyzing the sensor signal in the interval $(t_p, t_p + t_0)$, one identifies the delay τ, representing the time-of-flight (TOF) taken by the wave to travel to the target and back. Knowing TOF and wave speed allows one to precisely determine the target position relative to the sensor. A short signal (pulse) is sent, and the echoes resulting from wave backscatter at the internal material flaws are detected [6]. Information regarding the geometric

shape, size, and orientation can be extracted from the patterns of ultrasonic backscatter echoes [7].

Current-technology phased arrays employ pressure waves generated through normal impingement on the material surface. Such phased arrays have shown clear advantages in the inspection of very thick specimens and in the sidewise inspection of thick slabs, where electronic beam scanning and focusing have produced significant improvements in inspection efficiency (Figure 1a). However, such phased arrays cannot be efficiently used in thin-wall structures because of the small relative thickness of such structures.

Ultrasonic inspection of thin-wall structures (e.g., aircraft shells, storage tanks, large pipes, etc.) is a time-consuming operation that requires meticulous through-the-thickness C-scans of large areas. One method of increasing the efficiency of thin-wall structure' inspection is to utilize guided waves (e.g., Lamb waves in thin plates) instead of the conventional pressure waves [2,8–10]. Guided waves propagate inside thin-wall plates and shallow shells parallel to the midsurface. They can travel large distances with very little amplitude loss. Traditionally, guided waves have been generated by impinging the plate obliquely with a tone-burst from a relatively large ultrasonic transducer [11]. Snell's law ensures mode conversion at the interface, hence a combination of pressure and shear waves are simultaneously generated into the thin plate. The constructive and destructive interference of the pressure and shear waves generate the thicknesswise standing wave pattern that characterizes the guided waves. Deutsch et al. [12] demonstrated a phased array for the Lamb wave inspection of thin plates utilizing wedge-coupled conventional ultrasonic transducers and elaborated electronics. Steering and focusing of the Lamb waves beam were demonstrated. Potential applications of this method can be found in the wide-area ultrasonic inspection of aircraft, missiles, pressure vessels, oil tanks, pipelines, etc. Another method for guided waves generation is the comb transducer, which consists of a linear array of ultrasonic transducers that are fired consecutively. With this method, the generated waves tend to stay in a narrow beam aligned with the array axis. Tuning of the comb transducer element spacing and the

excitation frequency permits the selection of the appropriate guided wave mode most suitable for the desired application [13–15].

Though the Lamb wave-phased array methods are promising, the fact that they utilize conventional ultrasonic transducers, which are bulky and expensive, may make them unsuitable for structural health monitoring (SHM). Three reasons are apparent: (i) size and weight, (ii) cost, and (iii) principle of operation. Conventional ultrasonic transducers are resonant devices that consist of a piezoelectric oscillator disk, a protective layer, and a damping block. When activated, they generate high-frequency oscillations that impinge perpendicular to the contact surface. To generate an oblique incident wave, a wedge interface needs to be employed. Due to their internal complexity, conventional ultrasonic transducers are relatively bulky and expensive. It seems impractical and costly to conceive an SHM system based on conventional ultrasonic transducers permanently installed in an aircraft structure in a number sufficient to achieve the required structural coverage. However, this might be possible if a different class of transducers, which are both small and inexpensive, were available [16].

The advent of commercially available, low-cost piezoceramics has opened new opportunities for ultrasonic testing. The piezoelectric wafer active sensors (PWAS) have the potential for *in situ* ultrasonics through inexpensive and unobtrusive deployment [17]. Early work has shown that PWAS devices can successfully generate Lamb waves in thin-wall composite structures [18–20] as well as in metallic structures [21]. The present paper shows that these devices can be also utilized as phased arrays in the form of *embedded-ultrasonics structural radar* (EUSR) [22]. The EUSR concept consists of (a) a PWAS array embedded onto the structure, and (b) electronic modules for signal transmission/reception, processing, and interpretation. Due to its low cost, small size, and unobtrusiveness, the EUSR concept based on PWAS transducers seems better suited for *in situ* SHM of thin-wall structures than conventional ultrasonic transducers. The EUSR methodology was developed as an extension of our previous work on PWAS-generated Lamb wave SHM [21]. This paper

starts with the general principles of the EUSR concept, then describes developmental work on PWAS-generated Lamb waves, and ends with the presentation of the EUSR system design, calibration, and experimental testing.

2   Embedded-Ultrasonic Structural Radar (EUSR)

Embedded-ultrasonic structural radar is a concept that utilizes the phased-array radar principles and ultrasonic guided waves (Lamb waves) to scan large surface areas of thin-wall structures for the detection of cracks and corrosion defects [22]. In the EUSR concept, the guided Lamb waves are generated with surface-mounted PWAS. The guided Lamb waves have the property of staying confined inside the walls of a thin-wall structure. Hence, they can travel over large distances with little attenuation. In addition, they can travel inside curved walls with shallow curvature. The target location is described by the radial position, R, and the azimuth angle, ϕ. In conventional radars, the radar dish sweeps the horizon with a search beam that registers an echo when a target is detected. The phased-array radar replaces the rotating radar dish with an array of M active sensors that are electronically switched such as to generate a virtual sweep beam. The EUSR algorithm is adopted from the beam-forming process currently used in phased-array radar applications. Consider a PWAS array as presented in Figure 2(a). Each element in the PWAS array plays the role of both transmitter and receiver. The role of each PWAS is changed in a round-robin fashion by a methodology designed for that purpose. The responses of the structure to all the excitation signals are collected. By applying the EUSR algorithm, an appropriate delay is applied to each signal in the data set to make them all focus on a direction denoted by angle ϕ. When this angle ϕ is changed from 0 to 180°, a virtual scanning beam is formed and a large area of the structure can be interrogated (Figure 2(b)).

Lamb waves can exist in a number of dispersive modes. However, through smoothed tone-burst excitation and frequency tuning, it is possible to confine the excitation to a particular Lamb wave mode, of carrier frequency F_c, wave speed c, and wave length $\lambda = c/F_c$. Hence, the smoothed tone-burst signal generated by one PWAS is assumed of the form:

$$s_T(t) = s_0(t)\cos(2\pi F_c t), \quad 0 < t < t_p \qquad (1)$$

where $s_0(t)$ is a short-duration smoothing window that is applied to the carrier signal of frequency F_c between 0 and t_p. As in conventional phased-array radar, we assume a uniform linear array of M active sensors (PWAS), with each PWAS acting as a pointwise omnidirectional transmitter and receiver. The PWAS in the array are spaced at a distance d, which is assumed much smaller than the distance r to a generic, far-distance point, P. Since $d \ll r$, the rays joining the sensors with the point P can be assimilated with a parallel fascicle, of azimuth ϕ (Figure 2(a)).

Because of the array spacing, the distance between one PWAS and the generic point P will be different from the distance between another PWAS and P. For the mth PWAS, the distance will be shortened by $m(d\cos\phi)$. If all the PWAS are fired simultaneously, the signal from the mth PWAS will arrive at P quicker by $\Delta_m(\phi) = m(d\cos\phi)/c$. If the PWAS are not fired simultaneously, but with some individual delays, δ_m, $m = 0, 1, \ldots, M-1$, then the total signal received at point P will be

$$s_p(t) = \frac{1}{\sqrt{r}} \sum_{m=0}^{M-1} s_T\left(t - \frac{r}{c} + \Delta_m(\phi) - \delta_m\right) \qquad (2)$$

where $1/\sqrt{r}$ represents the decrease in the wave amplitude due to the omnidirectional 2-D radiation, and r/c is the delay due to the travel distance between the reference PWAS ($m = 0$) and the point P. (Wave-energy conservation, i.e., no dissipation, is assumed.)

2.1   Transmitter Beamforming

Beamforming at angle ϕ_0 with an array of M omnidirectional sensors is based on the principles of constructive interference in the fascicle of parallel rays emanating from the array. The
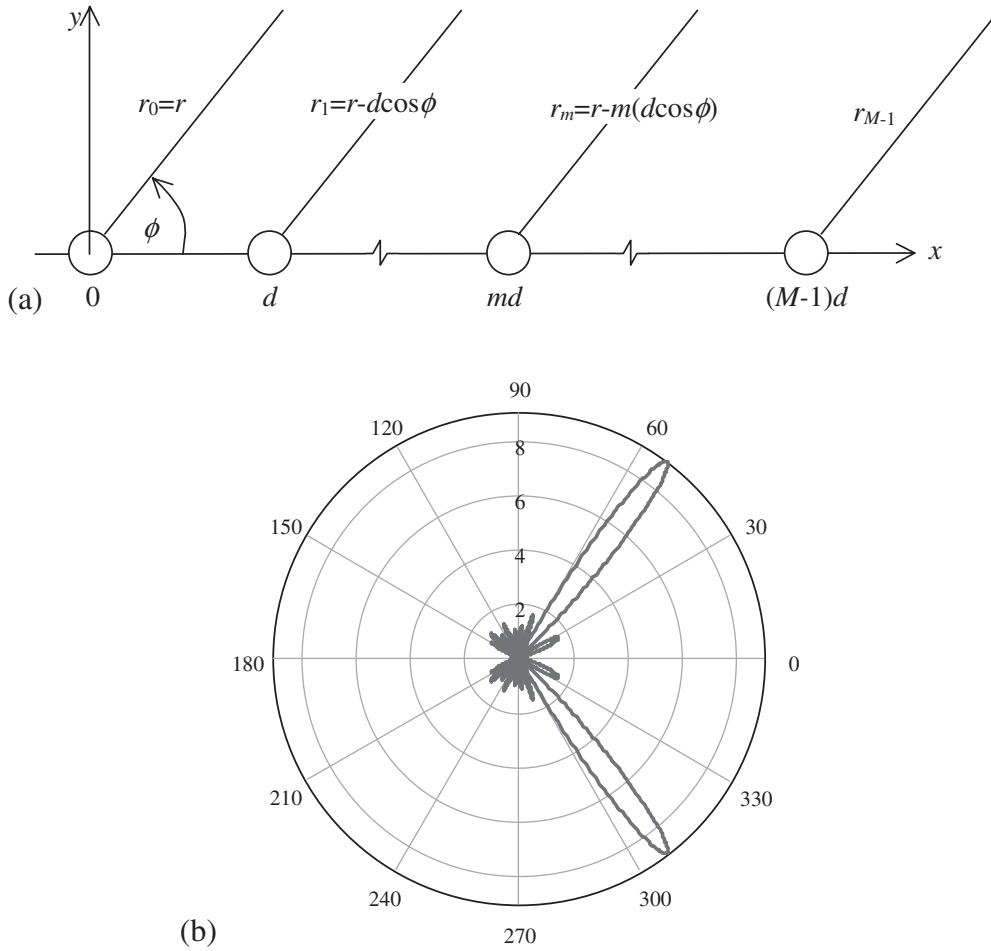
Figure 2 (a) Uniform linear array of *M* omindirectional active sensors spaced at pitch *d*; (b) calculated beamforming pattern for a 9-sensor array (spacing $l = \lambda/2$) with 53° target azimuth.

simplest way of achieving constructive interferences is to have $\delta_m = m\Delta(\phi)$, such that Equation (2) becomes

$$s_p(t) = M \cdot \frac{1}{\sqrt{r}} s_T\left(t - \frac{r}{c}\right) \qquad (3)$$

i.e. an *M* times increase in the signal strength with respect to a simple sensor. This leads directly to the beamforming principle, i.e., if $\delta_m = m(d/c)\cos(\phi_0)$, and since $\Delta_m = m(d/c)\cos(\phi)$, then constructive interference (beamforming) takes place when $\cos(\phi) = \cos(\phi_0)$, i.e. at angles $\phi = \phi_0$ and $\phi = -\phi_0$. Thus, the forming of a beam at angles ϕ_0 and $-\phi_0$ is achieved through delays in the firing of the sensors in the array. Figure 2(b) shows the beamforming pattern for $\phi_0 = 53°$.

2.2 Receiver Beamforming

The receiver beamforming principles are reciprocal to those of the transmitter beamforming. If the point P is an omnidirectional source at azimuth ϕ_0, then the signals received at the *m*th sensor will arrive quicker by $m\Delta_0(\phi) = m(d\cos\phi_0)/c$. Hence, we can synchronize the signals received at all the sensors by delaying them by $\delta_m(\phi_0) = m(d/c)\cos(\phi_0)$.

2.3 Phased-array Pulse-echo

Assume that a target exists at azimuth ϕ_0 and distance *R*. The transmitter beamformer is sweeping the azimuth in increasing angles ϕ and receives an echo when $\phi = \phi_0$. The echo will be

received on all sensors, but the signals will not be in synch. To synchronize the sensors signals, the delays $\delta_m(\phi_0) = m(d/c)\cos(\phi_0)$ need to be applied. The process is as follows. The signal sent by the transmitter beamformer is an M times boost of the original signal

$$s_p(t) = \frac{M}{\sqrt{R}} s_T\left(t - \frac{2R}{c}\right) \qquad (4)$$

At the target, the signal is backscattered with a backscatter coefficient, A. Hence, the signal received at each sensor will be $(A \cdot M/R)s_T \times (t - 2R/c + \Delta_m(\phi))$. The receiver beamformer assembles the signals from all the sensors with the appropriate time delays, i.e.,

$$s_R(t) = \frac{A \cdot M}{R} \sum_{m=0}^{M-1} s_T\left(t - \frac{2R}{c} + \Delta_m(\phi) - \delta_m\right) \quad (5)$$

Constructive interference between the received signals is achieved when $\delta_m = m(d/c)\cos(\phi_0)$. Thus, the assembled receive signal will be again boosted M times, with respect to the individual sensors, i.e.,

$$s_R(t) = \frac{A \cdot M^2}{R} \sum_{m=0}^{M-1} s_T\left(t - \frac{2R}{c}\right) \qquad (6)$$

The time delay between the receive signal, $s_R(t)$ and the transmit signal, $s_T(t)$ is

$$\tau = \frac{2R}{c} \qquad (7)$$

Measurement of the time delay τ observed in $s_R(t)$ allows one to calculate the target range, $R = c\tau/2$.

2.4 Practical Implementation of the EUSR Algorithm

The practical implementation of the signal generation and collection algorithms is described next. In a round-robin fashion, one active sensor at a time is activated as transmitter. The reflected signals are received at all the sensors. The activated sensor acts in pulse-echo mode, i.e. as both transmitter and receiver; the other sensors act as passive sensors. Thus, an $M \times M$ matrix of elemental signals is generated (Table 1). The elemental signals are assembled into synthetic beamforming responses using the synthetic beamformer algorithm given by Equations (2) and (3). The delays, δ_j, are selected in such a way as to steer the interrogation beam at a certain angle, ϕ_0. The synthetic-beam sensor responses, $w_i(t)$, synthesized for a transmitter beam with angle ϕ_0, are assembled by the receiver beamformer into the total received signal, $s_R(t)$, using the same delay as for the transmitter beamformer. However, to apply this method directly, one needs to know the target angle ϕ_0. Since, in general applications, the target angle is not known, we need to use an inverse approach: we write the received signal as a function of the parameter ϕ_0, using the array unit delay for the direction ϕ_0 as $\Delta_0(\phi_0) = (d/c)\cos\phi_0$. (To accurately implement the time shifts when the time values fall in between the fixed values of the sampled time, we have used a spline interpolation algorithm.)

Table 1 $M \times M$ matrix of elemental signals generated in a round-robin activation of the PWAS array elements.

Receivers	*Transmitters*				*Synthetic beamforming response*
	T_0	T_1		T_{M-1}	
R_0	$P_{0,0}(t)$	$P_{0,1}(t)$	$\ldots$	$P_{0,M-1}(t)$	$w_0(t)$
R_1	$P_{1,0}(t)$	$P_{1,1}(t)$	$\ldots$	$P_{1,M-1}(t)$	$w_1(t)$
R_2	$P_{2,0}(t)$	$P_{2,1}(t)$	$\ldots$	$P_{2,M-1}(t)$	$w_2(t)$
$\ldots$	$\ldots$	$\ldots$	$\ldots$	$\ldots$	$\ldots$
R_{M-1}	$P_{M-1,0}(t)$	$P_{M-1,1}(t)$	$\ldots$	$P_{M-1,M-1}(t)$	$w_{M-1}(t)$

A coarse estimate of the target direction is obtained by using an azimuth sweep technique, in which the beam angle, ϕ_0, is modified until the maximum received energy is attained, i.e.,

$$\max E_R(\phi_0), \quad E_R(\phi_0) = \int_{t_p}^{t_p+t_0} |s_R(t, \phi_0)|^2 \, dt \quad (8)$$

After a coarse estimate of the target direction is found ϕ_0, the actual round-trip time-of-flight, τ_{TOF}, is calculated using an optimal estimator, e.g., the cross-correlation between the receiver and the transmitter signals

$$y(\tau) = \int_{t_p}^{t_p+t_0} s_R(t) s_T(t - \tau) \, dt \quad (9)$$

Then, the estimated $\tau_{TOF} = 2R/c$ is obtained as the value of τ where $y(\tau)$ is maximum. Hence, the estimated target distance is

$$R_{exp} = c\tau_{TOF}/2 \quad (10)$$

This algorithm works best for targets in the far field, for which the "parallel-rays" assumption holds. For targets in the near and intermediate field, a more sophisticated self-focusing algorithm that uses triangulation principles can be used. This algorithm is an outgrowth of the passive-sensors target-localization methodologies [5]. The self-focusing algorithm modifies the delay times for each synthetic-beam response, $w_i(t)$, such that it maximizes the total response by finding the focal point of individual responses, i.e., the common location of the defect that generated the echoes recorded at each sensor. For very close range targets, SAFT techniques [23] can be utilized.

3 PWAS-generated Lamb Waves

The success of the EUSR concept rests on the ability of transmitting and receiving good quality Lamb waves using the PWAS technology. Hence, considerable effort was dedicated to studying the interaction between PWAS and the thin-wall structure during the Lamb-wave generation and detection, as well as to finding the optimum excitation frequency and calibrating the Lamb wave group velocity.

3.1 Review of Lamb Waves Principles

Lamb waves are guided waves that propagate inside thin-wall plates and shallow shells [24]. As guided waves, Lamb waves propagate parallel to the plate mid-surface and travel large distances with very little amplitude loss. Across the material thickness, Lamb waves present stationary wave patterns (Figure 3). Lamb waves can be either symmetric or anti-symmetric across the material thickness (S_n and A_n, respectively, where n represents the number of inflection points across the material thickness). The Lamb wave phase velocity, c_L, depends on the product of frequency, $f = \omega/2\pi$, and the material thickness, $h = 2d$. Since the wave speed varies with frequency, the propagation of Lamb waves is essentially dispersive. The dispersion curves can be obtained by solving the Rayleigh–Lamb frequency equation [25]. Define $\xi = (c_S^2/c_P^2)^{1/2}$, $\zeta = (c_S^2/c_L^2)^{1/2}$, $k_L = \omega/c_L$, $q = (k_L^2 - k_P^2)^{1/2}$, $s = (k_L^2 - k_S^2)^{1/2}$, where c_P is the pressure (longitudinal motion) wave velocity, c_S is the shear (transverse motion) wave velocity, and c_L is the Lamb wave velocity. For symmetrical motion (Figure 3(a)), one solves the Rayleigh–Lamb frequency equation in the form

$$\frac{\tan(\sqrt{1 - \zeta^2}\bar{d})}{\tan(\sqrt{\xi^2 - \zeta^2})} + \frac{4\zeta^2\sqrt{1 - \zeta^2}\sqrt{\xi^2 - \zeta^2}}{(2\zeta^2 - 1)^2} = 0 \quad (11)$$

Hence, the two components of the displacement can be expressed as [25]:

$$U(x, z, t)$$
$$= \text{Re}\left[Ak_L \left(\frac{\cosh(qz)}{\sinh(qd)} - \frac{2qs}{k_L^2 + s^2} \frac{\cosh(sz)}{\sinh(sd)} \right) e^{i(k_L x - \omega t - \frac{\pi}{2})} \right] \quad (12)$$

$$W(x, z, t)$$
$$= \text{Re}\left[Aq \left(\frac{\sinh(qz)}{\sinh(qd)} - \frac{2k_L^2}{k_L^2 + s^2} \frac{\sinh(sz)}{\sinh(sd)} \right) e^{i(k_L x - \omega t)} \right] \quad (13)$$
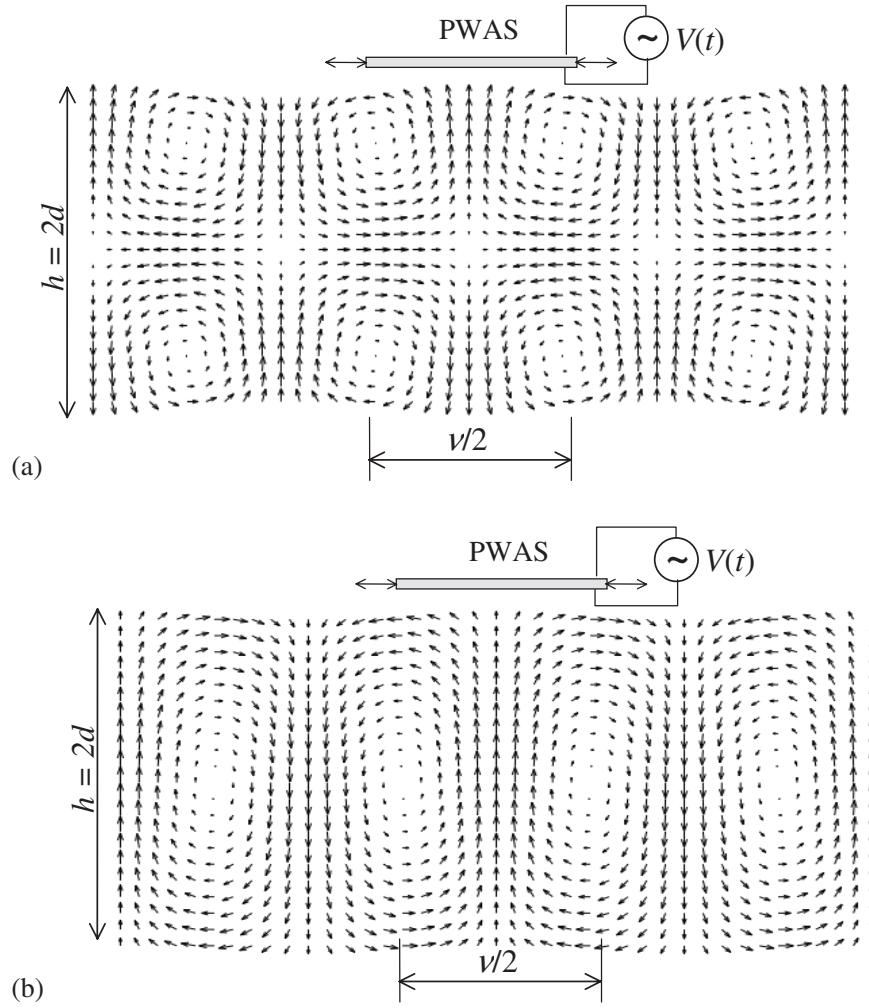
Figure 3 Simulation of Lamb wave motion in a 1-mm thick aluminum plate: (a) symmetric mode S_0, $f = 1.56$ MHz; (b) anti-symmetric mode A_0, $f = 0.788$ MHz. For full animation, see http://www.engr.sc.edu/research/lamss/default.htm under research Thrust 1.

For anti-symmetric motion (Figure 3(b)), the Rayleigh–Lamb frequency equation takes the form

$$\frac{\tan(\sqrt{1 - \zeta^2}\,\bar{d})}{\tan(\sqrt{\xi^2 - \zeta^2})} + \frac{(2\zeta^2 - 1)^2}{4\zeta^2\sqrt{1 - \zeta^2}\sqrt{\xi^2 - \zeta^2}} = 0 \quad (14)$$

and the two components of the displacement can be expressed as

$$U(x,z,t)$$
$$= \mathrm{Re}\left[Ak_L\left(\frac{\cosh(qz)}{\cosh(qd)} - \frac{2qs}{k_L^2 + s^2}\frac{\cosh(sz)}{\cosh(sd)}\right)e^{i(k_L x - \omega t - \frac{\pi}{2})}\right]$$
$$\quad (15)$$

$$W(x,z,t)$$
$$= \mathrm{Re}\left[Aq\left(\frac{\sinh(qz)}{\cosh(qd)} - \frac{2k_L^2}{k_L^2 + s^2}\frac{\sinh(sz)}{\cosh(sd)}\right)e^{i(k_L x - \omega t)}\right]$$
$$\quad (16)$$

The Lamb waves group velocity represents the speed with which Lamb wave packs are sent and received along the thin-wall plate. According to Rose [2]

$$c_g = c^2\left[c - (fd)\frac{\mathrm{d}c}{\mathrm{d}(fd)}\right]^{-1} \quad (17)$$
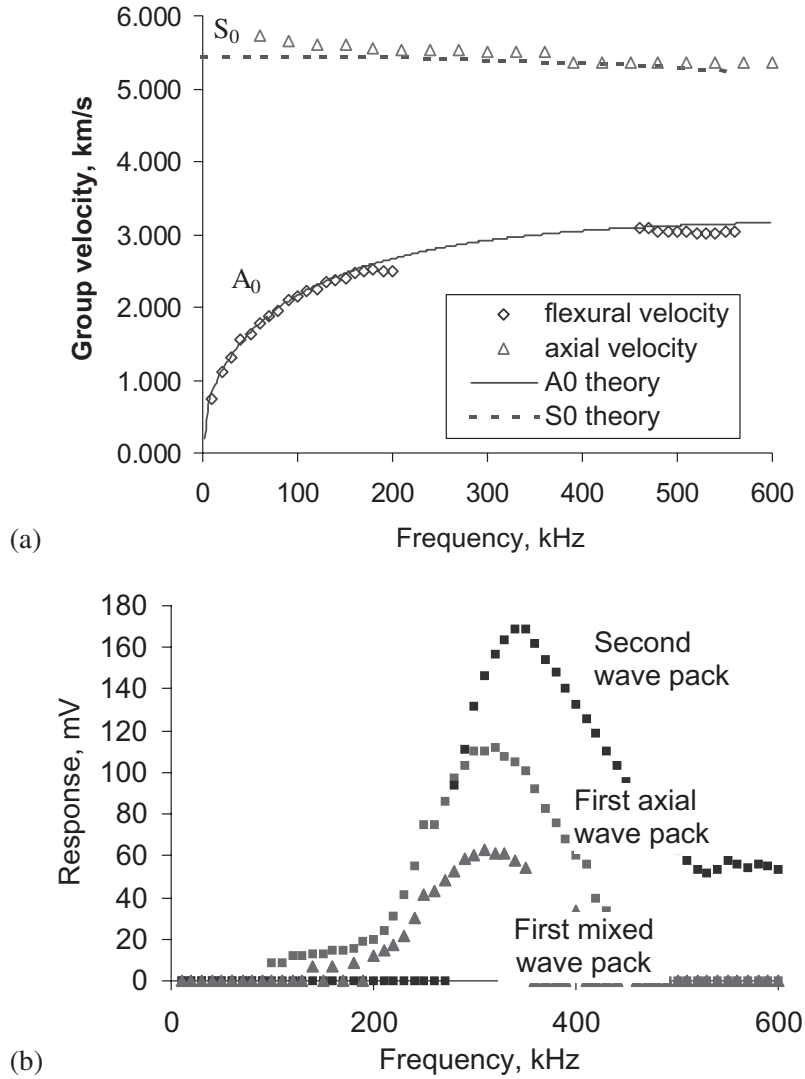
(a)

(b)

Figure 4   Verification that PWAS can excite Lamb waves over a wide frequency range: (a) group velocity dispersion curves for Lamb wave A_0 and S_0 modes, theory vs. experiment; (b) excitation "sweet spot" for S_0 axial mode identified through frequency tuning around 300 kHz.

where c_g is the group velocity, and c is the phase velocity. Thus, we calculated the Lamb wave group velocities dispersion curves for our specimens (Figure 4(a)).

3.2   PWAS Generation of Lamb Waves

Piezoelectric wafer active sensors are small wafers of piezoelectric material that are permanently bonded to the material surface and can simulta-

neously act as elastic-wave transmitters and receptors. PWAS are *strain transducers* that couple directly with the surface strains of the thin-wall structure. Due to the in-plane surface coupling, PWAS are ideally suited for the generation of guided plate waves (Lamb waves). Figure 3 shows how a surface-mounted PWAS can simultaneously excite both axial (S_0) and flexural (A_0) Lamb waves. For efficient Lamb-wave excitation, the PWAS length, l_a, must be an integer multiple of the Lamb wave half-length, $\lambda/2$, i.e., $l_a = k\lambda/$

$2, k = 1, 2, \ldots$ When a time-varying voltage, $V(t)$, is applied to the PWAS electrodes, the PWAS expands and contracts in accordance with the laws of piezoelectricity. Thus, the PWAS acts as a Lamb wave generator. Conversely, when a Lamb wave is present in the material under a PWAS, the surface expansions and contractions are felt by the PWAS and transformed in time-varying electric signals. In this case, the PWAS acts as a wave sensor. Of particular importance is the fact that PWAS are coupled with the material strains parallel to the material surface. Thus, transmission and reception of Lamb waves in thin-wall structures are greatly facilitated. This type of coupling, which is parallel to the material surface, is significantly more efficient for the excitation and reception of Lamb waves than that of the conventional ultrasonic transducers, which can only impinge normal to the material surface (or at an angle, when using wedge couplers). This observation, in addition to the much lower cost of PWAS transducers, highlights their advantage over conventional ultrasonic transducers in the transmission and reception of Lamb waves.

3.3   Calibration of PWAS-generated Lamb Waves

Before attempting to use PWAS in the implementation of the EUSR concept, several calibration experiments were conducted to verify that: (a) Lamb waves could be satisfactorily generated and detected with PWAS; (b) the generated Lamb waves are omnidirectional; and (c) the group velocity satisfies the theoretical predictions. Of particular interest was to prove that the amplitude of the generated waves was sufficiently strong such that perceivable echoes could be received, since the PWAS are an order of magnitude smaller and lighter than conventional ultrasonic transducers. In addition, of special interest was to prove that the Lamb waves generated by PWAS are omnidirectional, since some guided waves generated with conventional ultrasonic transducers and wedge converters were reported not to be omnidirectional, but rather confined to narrow beams [26].

A 1.6-mm thick, 2024-aluminum alloy rectangular plate (914 mm × 504 mm × 1.6 mm) was instrumented with eleven 7-mm square, 0.2-mm thick piezoelectric wafers (American Piezo Ceramics Inc., APC-850). The sensor locations are given in Table 2. The sensors were connected with thin insulated wires to a 16-channel signal bus and two 8-pin connectors. An HP33120A signal generator was used to generate Hanning-windowed tone-burst excitation of 10-V amplitude of various frequencies and 10 Hz repetition rate. A Tektronix TDS210 two-channel digital oscilloscope, synchronized with the signal generator, was used to collect the response signals. One of the oscilloscope channels collected the signal from the transmitter PWAS, while the other channel was switched among the remaining PWAS using a digitally controlled switching unit. A National Instruments LabView™ data acquisition program was developed to control the signal switching and to download and process the data from the digital oscilloscope. To precisely determine the TOF, the raw signals were processed using a narrow-band signal correlation followed by envelope detection. In addition, a Motorola MC68HC11 microcontroller was tested as an embedded stand-alone controlling option.

3.3.1 Experimental Determination of Group Velocity Dispersion Curves The experimental

Table 2   Locations of the 11 PWAS on the thin rectangular plate specimen and the time of arrival of a 300 kHz S_0 Lamb wave transmitted omnidirectionally by PWAS #11 and received at PWAS #1–8 ($r_{\#11}$ = distance from transmitter PWAS #11).

PWAS #	1	2	3	4	5	6	7	8	9	10	11
x (mm)	100	100	100	100	100	450	450	450	800	800	800
y (mm)	100	175	250	325	400	100	250	400	100	250	400
$r_{r\#11}$ (mm)	761.6	735.3	715.9	704.0	700.0	461.0	380.8	350.0	300.0	150.0	0

determination of the group velocity dispersion curves was performed in the pitch-catch mode, using one PWAS as a transmitter and another as a receiver. Since PWAS placed on only one side of the plate simultaneously excite symmetric and antisymmetric Lamb waves, two wave packs were simultaneously observed on the received signal trace. First the S_0 axial waves, then the A_0 flexural waves. Below 200 kHz and above 450 kHz, the A_0 waves were stronger and easier to observe than the S_0 waves. However, in the interval 200–450 kHz, the S_0 waves became dominant, and the A_0 waves could not be properly excited. By processing the TOF–distance information, the group velocity could be determined. Figure 4a shows the plot of group velocity versus frequency, as resulted from our measurements. The theoretical values obtained by solving Equations (11), (14), and (17) are plotted too. The concordance between the theoretical A_0 group velocity and the measured A_0 group velocity is remarkably good. The S_0 signals also show good concordance with the theoretical predictions, except at low frequencies ($f < 100$ kHz) where the excitation of axial waves is more difficult due to the flexural wave's dominance. Overall, the data presented in Figure 4(a) indicate that the theoretically predicted Lamb wave group velocities could be successfully confirmed experimentally.

3.3.2 Frequency Tuning of Lamb Waves

Further investigation was devoted to the mentioned phenomenon, whereas in the range 200–450 kHz, the excitation of S_0 axial waves became dominant. By carefully stepping through the frequencies, it was observed that, as the frequency increases beyond 150 kHz, the excitation of flexural waves decreases, while that of axial waves increases. A "sweet spot" for axial wave excitation was found in the 300–400 kHz range. Figure 4(b) shows that, at 300 kHz, peak values of both the first mixed wave pack and the axial wave were observed. The second wave pack peaked at 350 kHz. This frequency-tuning effect was found to be of utter importance, since it presented us with the opportunity of exciting low-dispersion S_0 waves of strong intensity. Subsequently, for the rest of our experiments, the excitation at 300 kHz was adopted as standard.

3.3.3 Lamb Wave Omnidirectionality

To prove that the Lamb waves excited by PWAS are omni-directional, we used one PWAS (#11) as a transmitter and the other PWAS (#1–#10) as a receiver. The signals observed in this investigation are shown in Figure 5(a). In each row, the electromagnetic coupling of the 'initial bang' is shown around the origin. Then, the first wave package corresponding to the wave received from the transmitter PWAS is seen, followed by other wave packages corresponding to reflections from the plate edges. The time difference between the initial bang and the wave-package arrival represents the TOF. The TOF is consistent with the distance traveled by the wave. Figure 5(b) shows the straight-line correlation between TOF and distance. The slope of this line is the experimental group velocity, $c_g = 5.446$ km/s. The theoretical value should be 5.440 km/s (Figure 3(a)). Very good accuracy is observed (99.99% correlation; 0.1% speed detection error). Thus, it was proved that the PWAS-generated Lamb waves propagate omnidirectionally with good detection and velocity resolution properties.

4 EUSR System Design and Experimental Validation

The EUSR system consists of three major modules: (a) the PWAS array; (b) the DAQ module; and (c) the signal-processing module. A system diagram is shown in Figure 6(a). A proof-of-concept EUSR system was built in the Laboratory for Active Materials and Smart Structures (LAMSS) at the University of South Carolina to evaluate the feasibility and capability of the EUSR system.

4.1 Experimental Setup

Three specimens were used in the experiments. These specimens were 1220-mm square panel of 1-mm thick 2024-T3 Al-clad aircraft grade sheet metal stock. One of the specimens (specimen #0) was pristine and was used to obtain baseline data. The other two specimens were manufactured with simulated cracks. The cracks were placed on a line midway between the center of the plate and
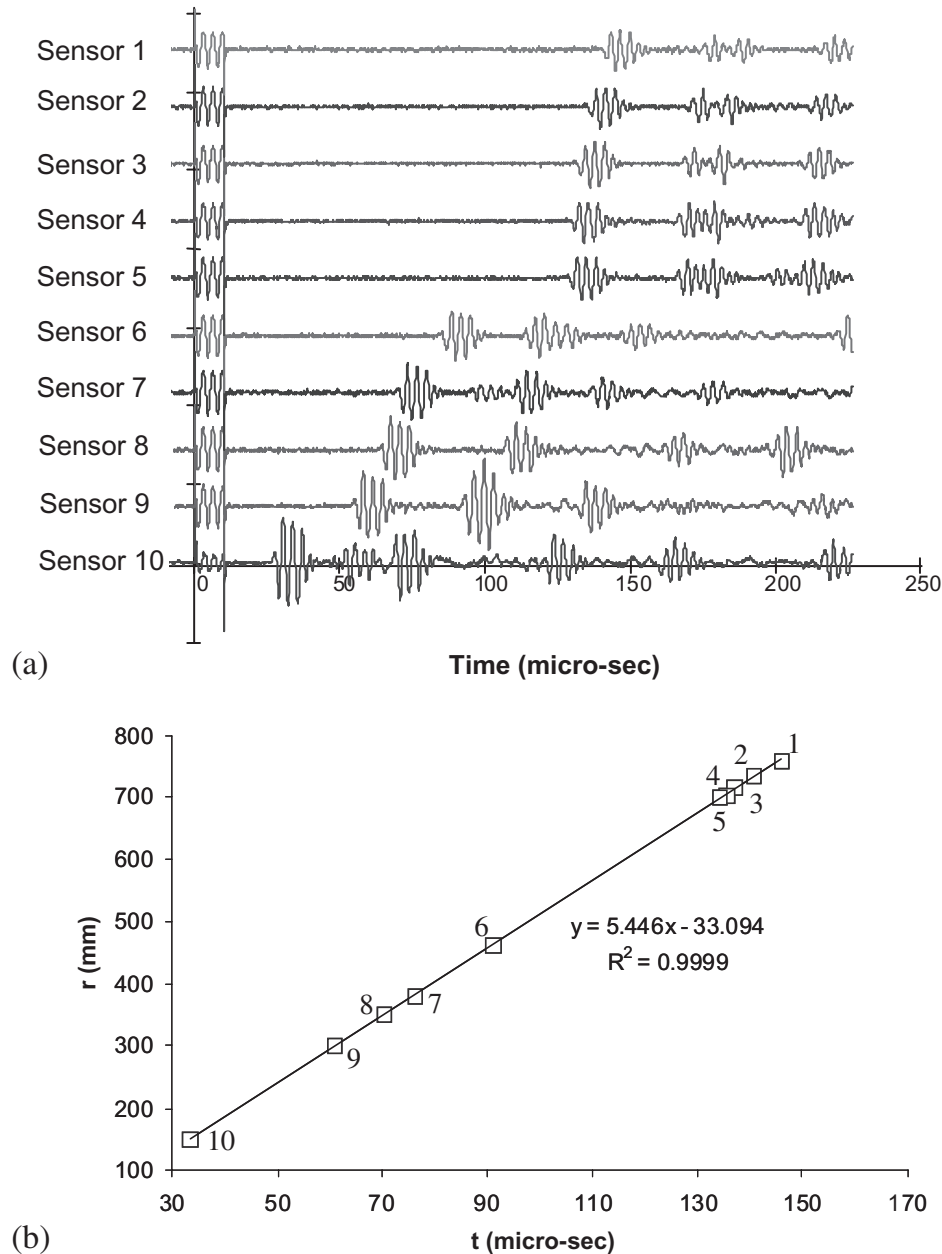
Figure 5 (a) Verification of Lamb-wave group velocity: (a) reception signals on PWAS #1–10 when a constant-amplitude tone-burst was applied to PWAS #11; (b) correlation between distance and TOF.

its upper edge (Figure 6(b)). The cracks were 19 mm long, 0.127 mm wide. On specimen #1, the crack was placed broadside w.r.t. the phase array, at coordinates (0, 0.305 m), i.e. at $R = 305$ mm, $\phi_0 = 90°$. On the specimen #2, the crack was placed offside w.r.t. the phased array, at coordinates $(-0.305 \text{ m}, 0.305 \text{ m})$, which corresponds to $R = 409$ mm, $\phi_0 = 136.3°$ w.r.t. the reference point

of the PWAS array. The PWAS array was constructed from nine 7 mm^2, 0.2-mm thick piezoelectric wafers (American Piezo Ceramic Inc., APC-850) placed on a straight line in the center of the plate. The sensors were spaced at pitch $d = \lambda/2$, where $\lambda = c/f$ is the wavelength of the guided wave propagating in the thin-wall structure. Since the first optimum excitation
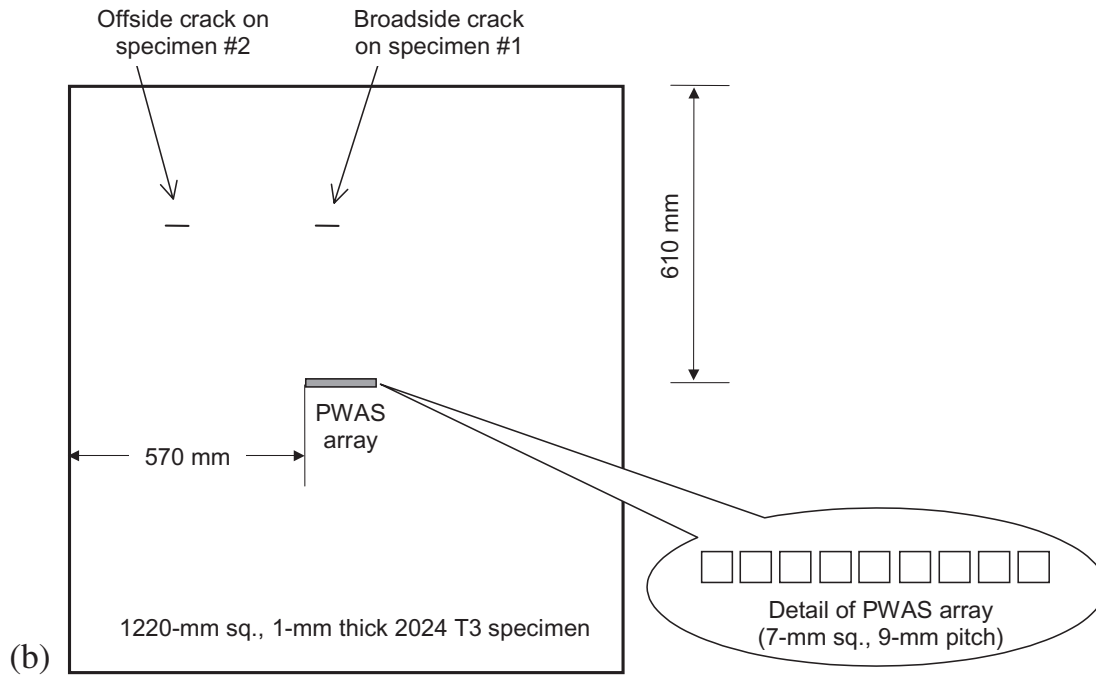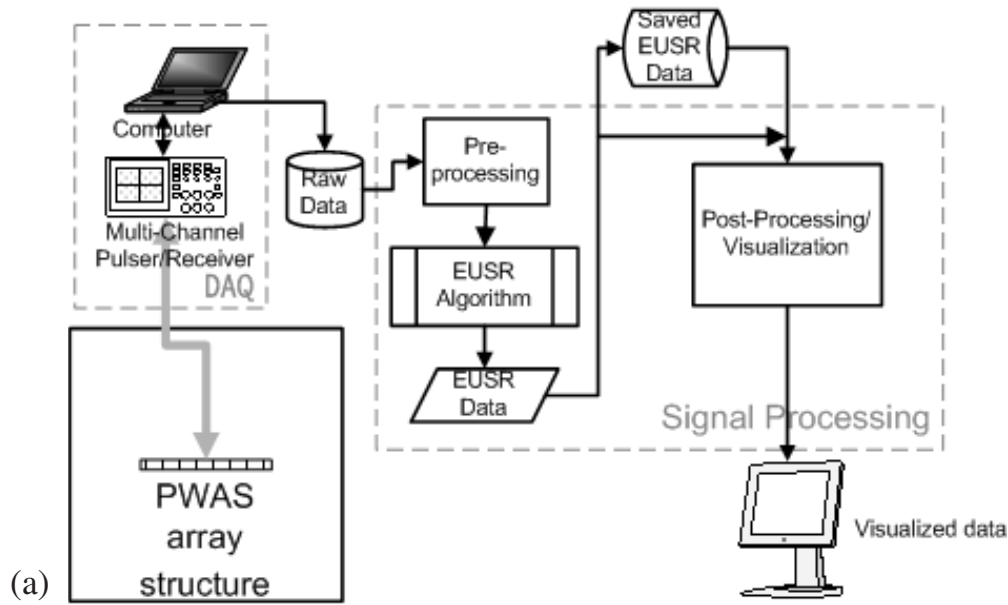
Figure 6 Proof-of-concept EUSR construction: (a) data flow diagram; (b) thin-plate specimens with broadside and offside cracks, and 9-element PWAS array at the center.

frequency for S_0 mode was 300 kHz, and the corresponding wave speed was $c = 5.440$ km/s, the wavelength was $= 18$ mm. Hence, the spacing in the PWAS array was selected as $d = 9$ mm (Figure 6(b)).

The DAQ module consisted of an HP33120A arbitrary signal generator, a Tektronix TDS210 digital oscilloscope, and a portable PC with DAQ and GPIB interfaces. The HP33120A arbitrary signal generator was used to generate a 300 kHz

Hanning-windowed tone-burst excitation with a 10 Hz repetition rate. Under the Hanning-windowed tone-burst excitation, one element in the PWAS array generated a Lamb waves package that spread out into the entire plate in an omnidirectional pattern (circular wave front). The Tektronix TDS210 digital oscilloscope, synchronized with the signal generator, collected the response signals from the PWAS array. One of the oscilloscope channels was connected to the transmitter PWAS, while the other was switched among the remaining elements in the PWAS array by using a digitally controlled switching unit. A LabVIEW^{TM} computer program was developed to digitally control the signal switching, to record the data from the digital oscilloscope, and

to generate the group of raw data files. Photographs of the experimental setup are presented in Figure 7.

4.2   Experimental Results

Both the broadside crack (specimen #1) and the offside crack (specimen #2) were successfully detected. However, the offside crack presented a detection challenge: because of the inclination of the crack with respect to the beam axis, the ultrasonic beam was deflected away from the phased array. The only signal received at the phased array was the faint backscatter generated by wave diffraction at the crack tips. This latter case, which is more challenging, will be discussed
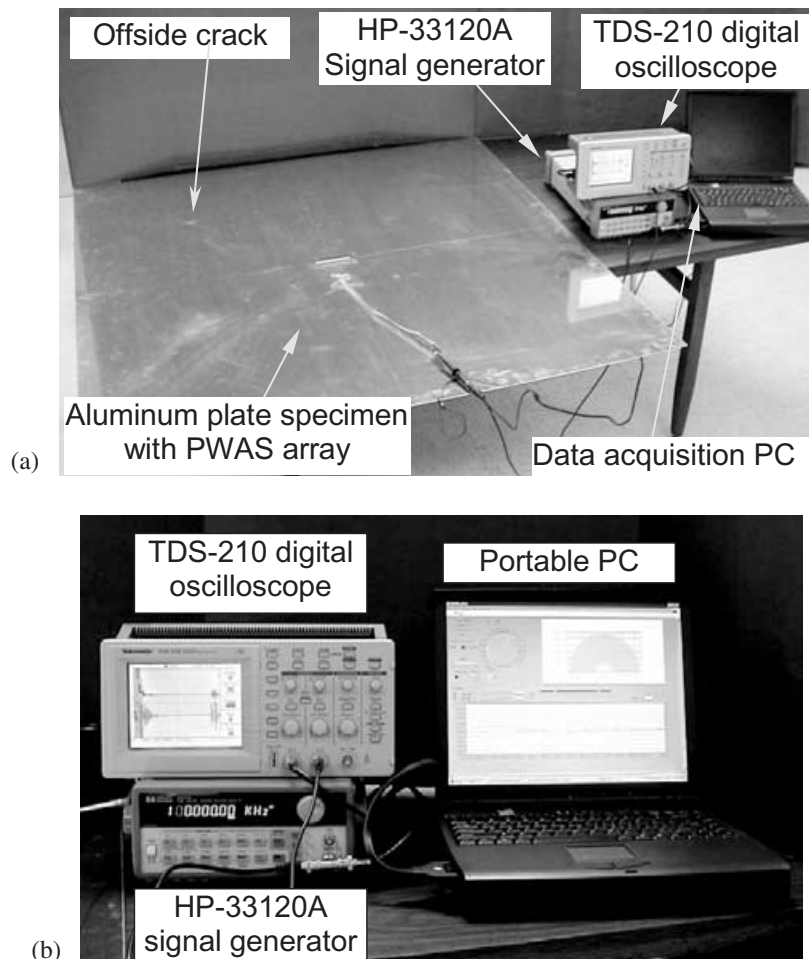

Figure 7   Experimental setup for EUSR experiment: (a) overall view showing the plate, active sensors, and instrumentation; (b) detail of the instrumentation and the data acquisition program.

here in detail. This discussion will illustrate the capabilities of the EUSR algorithm.

4.2.1 Constructive Interference of Sensors Signals The results for the offside crack experiment are shown in Figure 8(a). Presented are the original signal from one sensor and the EUSR reconstruction using information from all the array sensors. For display purpose, the signals were separated by applying a vertical shift. The original signal is shown at the top, and the reconstructed signal is shown at the bottom. The
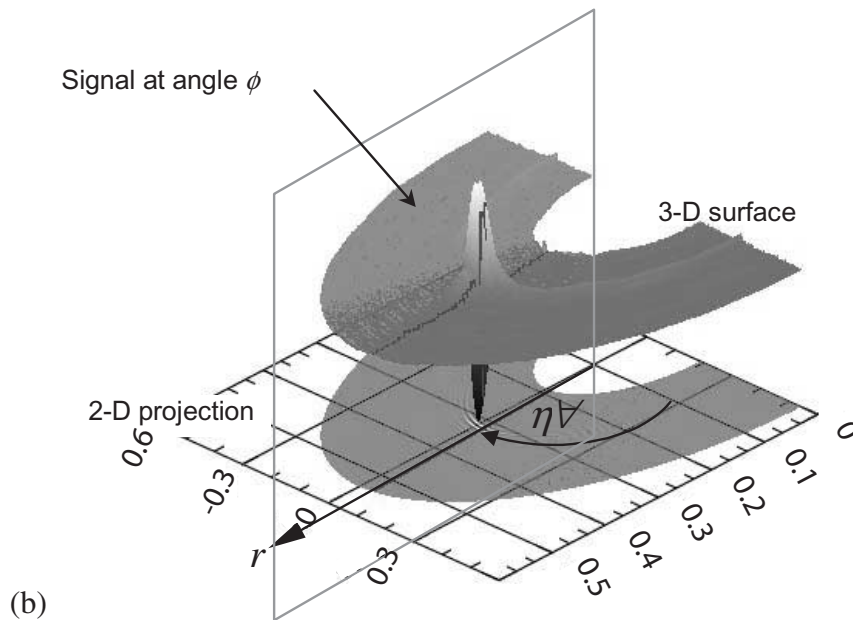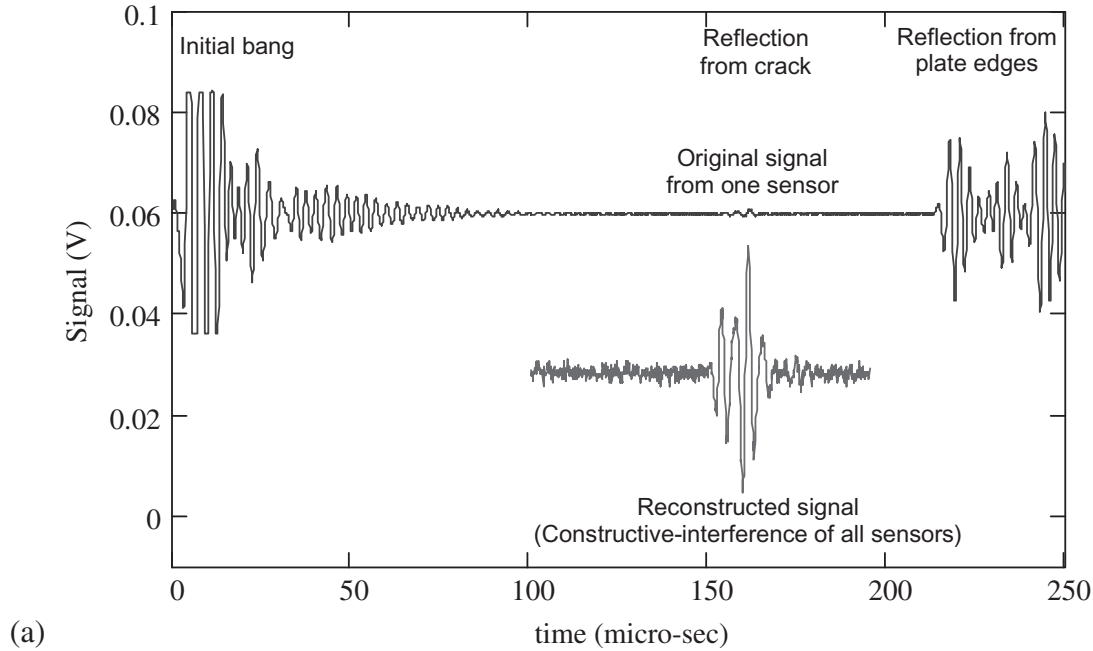

(a)

(b)

Figure 8 EUSR signal reconstruction examples: (a) very good signal enhancement through the EUSR phased-array method illustrated on the offside crack specimen #2; (b) 3-D visualization of EUSR signal reconstruction for the broadside crack specimen #1.

reconstructed signal was obtained by the constructive interference of all the original sensor signals, with the appropriate time delays, as described in Section 2 of this paper. One notices that the original sensor signal (top) displays a faint tremor at approximately 151 µs representing the backscatter from the offside crack. This tremor is very faint because the crack is positioned at such an angle that the ultrasonic interrogation beam is actually reflected away and to the left and does not come back to the PWAS array. What is received at the PWAS array are residual backscatter signals generated through wave diffraction at the crack. It is apparent that the signal-to-noise ratio (SNR) of the individual sensor signal is very poor. Obviously, the original sensor signals could not be used for crack detection. However, the SNR of the reconstructed signal, as enhanced through the EUSR algorithm, is at least one order of magnitude better. The enhanced signal can be used for crack detection. In this enhanced signal, the TOF of the crack signal is easily identified as $\tau_{\text{TOF,offside}} = 151$ µs. Using $c_g = 5.440$ mm/µs yields the range of the crack as $R_{\text{Offside}} = 411$ mm. The exact value is 409 mm, i.e., 0.4% error. The accuracy of the EUSR method seems very good.

4.2.2   Signal Processing   The signal-processing module reads the raw data files and processes them using the EUSR algorithm. Although the EUSR algorithm is computationally nonintensive, the large amount of data points in each signal made this step time-consuming. Hence, we selected to save the result of EUSR data processing on the PC for later retrieval. This approach also enables other programs to access the EUSR results. The results of EUSR algorithm processing is a collection of signals representing the structural response at different angles, as defined by the parameter ϕ. In other words, they represent the response when EUSR scanning beam turned at incremental angles ϕ.

After being processed, the data was transformed from the time domain to the 2-D physical domain. Knowing the Lamb wave speed c, and using $r = ct$, the EUSR signal was transformed from voltage V versus time t to voltage V versus distance r. The signal detected at angle ϕ was plotted on a 2-D plane at angle ϕ. Since angle ϕ was stepped from 0 to 180°, at constant increments, the plots covered a half space. These plots generate a 3-D surface, which is a direct mapping of the structure being interrogated, with the z value of the 3-D surface representing the detected signal at that (x, y) location (Figure 8(b)). If we present the z value on a color/grayscale, then the 3-D surface is projected to the 2-D plane, and the color/grayscale of each point on the plane represents the intensity of the reflections.

4.2.3   Defect Mapping Results   Figure 9 shows the EUSR detection visualization for the broadside crack (Figure 9(a)) and the offside crack (Figure 9(b)) specimens. The group velocity was used to map the EUSR data from time domain to the space domain; thus, the locations of the reflectors can be visually displayed. The grids represent exact mapping in meters. The shaded area represents the swept surface. The signal amplitude is presented on color/grayscale intensity scale. The location of the crack is easily determined from the color/grayscale change. Figure 9(a) presents the results for the broadside specimen. The small area with darker color represents high amplitude echo (reflected wave) generated when the scanning angular beam intercepted the crack. From the picture scale, we observe that this area is located at an angle of 90° and at approximately 0.3 m from the center of the plate. Careful analysis of the reconstructed signal yielded the exact $\tau_{\text{TOF,broadside}} = 112.4$ µs, corresponding to a radial position $R_{\text{broadside}} = 305.7$ mm. This differs a mere 0.2% from the actual position of the broadside crack on this specimen ($\phi_0 = 90°$, $R = 305$ mm). The dark area in the EUSR result predicted the simulated crack perfectly. Similarly, Figure 9(b) presents the results for the offside specimen. It is apparent that the offside crack is located just beyond the $(-0.3$ m, 0.3 m) coordinates, which compares very well with the actual values $(-0.305$ m, 0.305 m). The crack range $R_{\text{offside}} = 411$ mm, determined from the analysis of the reconstructed echo, showed 0.4% accuracy. Figures 8 and 9 prove that the detection sensitivity and accuracy of the EUSR method are extremely good.
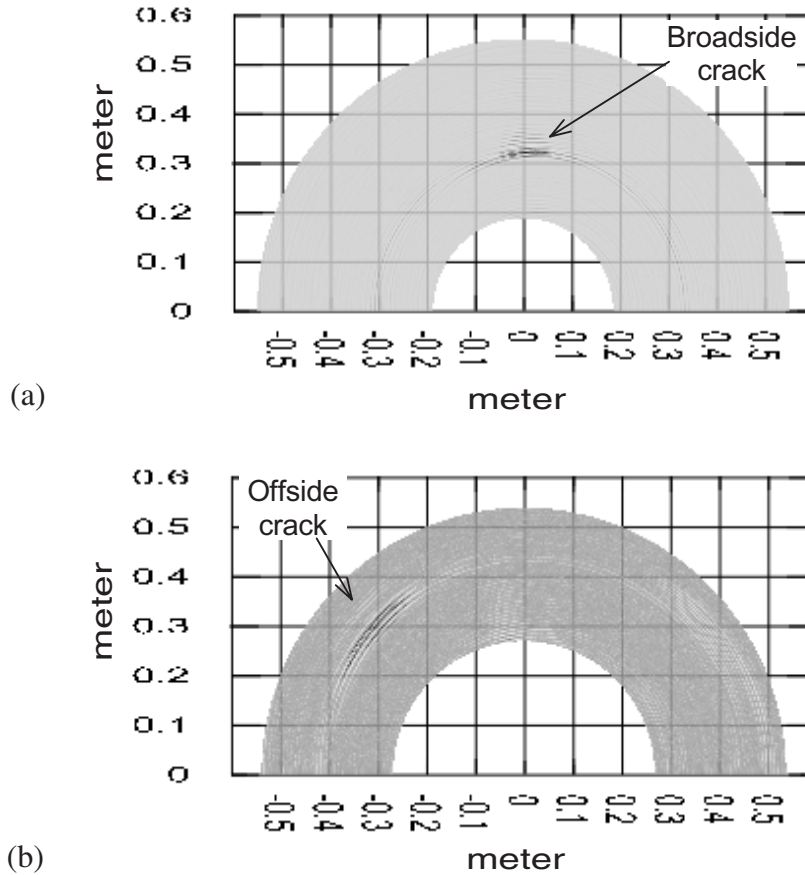
Figure 9 EUSR mapping results: (a) detection of a broadside crack ($\phi_0 = 90°$, $r = 305$ mm); (b) detection of an offside crack ($\phi_0 = 136.3°$, $r = 409$ mm).

4.2.4 Application of EUSR Concept to Complex Structures

It is important to explain how the EUSR system would work in the case of complex geometries that include splice joints, rivets, bolts, hinges, etc. In a separate work [27], the authors achieved the detection of cracks in complex geometries (but without the phased array) using the differential signal method. This method, specific to SHM applications, consists of a stored baseline signature signal measured in the pristine structure which contains the effects of the complex geometry without structural damage. Then, when structural damage is present, the signal changes. By taking the difference between the signal in the damaged structure and the baseline signal from the pristine structure, one obtains a signal that contains only the effect due to the structural damage. This method was used successfully in a realistic aircraft panel with a splice joint, stiffeners, doublers, and several rows of rivets [27]. The authors believe that the differential signal method could be directly applied to the EUSR phased-array concept.

5 Summary and Conclusions

This paper has presented a novel SHM concept – the embedded-ultrasonic structural radar EUSR [22]. The concept is novel because it combines the phased-array radar principles with the use of arrays of embedded PWAS that can simultaneously act as transmitters and receptors of omnidirectional Lamb waves in thin-wall structures. The sensors are considered "embedded" into the structure, since they are permanently

attached to the structure and can even be placed inside closed cavities such as wing structures. The PWAS can be left in place for life of the structure. The EUSR concept opens new horizons for performing *in situ* damage detection and SHM of a multitude of thin-wall structures such as aircraft, missiles, pressure vessels, oil tanks, pipelines, etc.

The systematic theoretical and experimental investigation presented in this paper has proved several essential points:

- First, it was shown that small (7 mm × 7 mm × 0.2 mm) PWAS could excite omnidirectional Lamb waves of sufficient amplitude for meaningful detection with conventional laboratory equipment. A frequency "sweet spot" was identified in the 300 kHz range where S_0 Lamb waves of very strong amplitude were excited. This was achieved through tuning the PWAS with the surface component of the S_0 Lamb wave modeshape.
- Secondly, it was shown that the same PWAS could simultaneously be used as both Lamb waves transmitter and Lamb waves receiver in thin aluminum plates. Though transmission was done with low-voltage signals (10 V pp), the captured signals were sufficiently strong (up to 50 mV pp) to be used directly in the signal-processing module without electronic amplification. It is conceivable that similar propagation will also happen in thin-gage shallow shells typical of aerospace structures.
- Thirdly, it was shown that the phased-array principles for transmission and reception beamforming could be successfully applied to PWAS-phased arrays using the EUSR concept. The proof-of-concept experiments described in this paper illustrate that the EUSR concept is able to detect both broadside and offside cracks. The detection of the offside crack was particularly challenging, since the crack was oriented at an odd angle with respect to the ultrasonic beam, and the beam was deflected away from the phased array. For this reason, in the elemental signals, the backscatter from this crack was barely noticeable. However, after the application of the signal reconstruction algorithm through the constructive

interference of the signals from all the nine sensors in the phased array, the crack signal became "loud and clear". Very good detection accuracy was observed for both the broadside and the offside cracks.

The original contributions of this paper can be summarized as follows:

1. The paper presents, for the first time, the application of phased-array technology to an array of small-weight low-power PWAS.
2. The paper presents, for the first time, the use of a phased array with only one excitation channel that is switched between the elements of the array in a round-robin fashion. The excitation is low-power, as needed in embedded applications. During the round-robin process, a set of N^2 elemental signals are collected.
3. The paper presents, for the first time, a method of virtual beam forming and focusing. The method uses a set of N^2 elemental signals, where N is the number of PWAS elements in the array, to assemble a virtual beam that can be steered and focused in virtual time using the graphical user interface of the EUSR algorithm.
4. The paper presents, for the first time, the use of a phased array in virtual time. The virtual time use of a phased array is appropriate to SHM applications, where the results are not required in real time since sufficient time is available to perform post processing of the data.
5. The paper presents, for the first time, experimental proofs that phased-array technology can be achieved with embedded PWAS and a single low-power excitation channel. This experimental proof is very important for embedded SHM applications, because it demonstrates how to reduce the hardware weight and cost of an SHM system while maintaining the functionality of conventional NDE methods.

The results reported in this paper indicate that the emerging field of *embedded-ultrasonics structural health monitoring* can be developed using proven phase-array ultrasonic testing methodologies that were initially designed for conventional ultrasonic transducers. The use of the small and inexpensive PWAS, instead of the relatively bulky

and costly conventional ultrasonic transducers, could permit the construction of embedded-ultrasonics SHM systems that can be applied to whole structures with very little weight and cost penalty. Though the EUSR experiments reported here were conducted on simple-geometry metallic plates, the findings of this study could be extended to practical geometries and to composite or hybrid-material structures. However, sustained theoretical research and technological development are needed to make the field of embedded ultrasonics realize its full potential.

Acknowledgments

References

1. Krautkramer, J. and Krautkramer, H. (1990). *Ultrasonic Testing of Materials*, Springer-Verlag.

2. Rose, J.L. (1999). *Ultrasonic Waves in Solid Media*, Cambridge University Press.

3. Krautkramer (2002). *Products Catalog*, http://www.krautkramer.com/arrayweb/default.htm

4. Lines, D. and Dickson, K. (1999). Optimization of high-frequency array technology for lap-joint inspection. In: *Proceedings of the 3rd Joint Conference on Aging Aircraft*.

5. Silvia, M.T. (1987). Time delay estimation. In: Elliot, D.F. (Ed.), *Handbook of Digital Signal Processing*, Academic Press.

6. Ravenscroft, F.A., Newton, K. and Scruby, C.B. (1991). Diffraction of ultrasound by cracks: comparison of experiment with theory, ultrasonics, (January 1991), *29*, 29–37.

7. Demirli, R. and Saniie, J. (2001). Model-based estimation of ultrasonic echoes. *IEEE Transactions of Ultrasonics, Ferroelectrics, and Frequency Control* (May 2001), *48(3)*, 787–811.

8. Krautkramer (1998). Emerging technology – guided wave ultrasonics. *NDTnet* (June 1998), *3(6)*.

9. Rose, J.L. (1995). Recent advances in guided wave NDE. *1995 IEEE Ultrasonics Symposium*, 761–770.

10. Rose, J.L. (2001). A vision of ultrasonic guided wave inspection potential. *Proceeding of the 7th ASME NDE Topical Conference*, NDE-Vol. 20, pp. 1–5.

11. Alleyne, D.N. and Cawley, P. (1992). Optimization of lamb wave inspection techniques. *NDTE International*, *25(1)*, 11–22.

12. Deutsch, W.A.K., Cheng, A. and Achenbach, J.D. (1998). Defect detection with Rayleigh and Lamb waves generated by a self-focusing phased array. *NDT.net* - December 1998, *3(12)*, http://www.ndt.net/article/ecndt98/steel/335/335.htm

13. Rose, J.L., Pelts, S.P. and Quarry, M.J. (1998). A comb transducer model for guided wave NDE, *Ultrasonics*, *36*, 163–169.

14. Alleyne, D.N., Pavlakovic, B., Lowe, M.J.S. and Cawley, P. (2001). Rapid, long range inspection of chemical plant pipework using guided waves. *Review of Progress in QNDE*, *20*, 180–187.

15. Wooh, S.-C. and Shi, Y. (2001). Synthetic phase tuning of guided waves. *IEEE Transactions of Ultrasonics, Ferroelectrics, and Frequency Control*, *48(1)*, 209–223.

16. Giurgiutiu, V. (2001). *In-situ Structural Health Monitoring, Diagnostics, and Prognostics System Utilizing Thin Piezoelectric Sensors*, USC-IPMO, Disclosure ID No. 20010001 of 01/24/2001, U.S. Patent Office Application Serial No. 10/072,644 of February 8, 2002, Attorney Docket No. 16139/09021.

17. Giurgiutiu, V. and Zagrai, A.N. (2001). Embedded self-sensing piezoelectric active sensors for on-line structural identification. *ASME Journal of Vibration and Acoustics*, *124*, 116–125.

18. Chang, F.-K. (1995). Built-in damage diagnostics for composite structures. *Proceedings of the 10th International Conference on Composite Structures (ICCM-10)*, Vol. 5 (pp. 283–289), Whistler, B. C., Canada, August 14–18, 1995.

19. Chang, F.-K. (1998). Manufacturing and design of built-in diagnostics for composite structures. *52nd Meeting of the Society for Machinery Failure Prevention Technology*, Virginia Beach, VA, March 30–April 3, 1998.

20. Chang, F.-K. (2001). Structural health monitoring: aerospace assessment. *Aero Mat 2001, 12th ASM Annual Advanced Aerospace Materials and Processes Conference*, Long Beach CA, 12–13 June 2001.

21. Giurgiutiu, V., Bao, J. and Zhao, W. (2001). Piezoelectric-wafer active-sensor embedded ultrasonics in beams and plates. *Experimental Mechanics*, Sage Pub., *43(4)*, December 2003, pp. 428–449.

22. Giurgiutiu, V. and Bao, J.J. (2002). Embedded-ultrasonics structural radar (EUSR) with piezoelectric-wafer active sensors (PWAS) for wide-area nondestructive evaluation of thin-wall structures, USC-IPMO, Disclosure ID No. 00327 of 02/13/2002.

23. Shandiz, H.T. and Gaydecki, P. (1999). A new SAFT method in ultrasonic imaging at very low frequencies by using pulse echo method, *NDTnet*, *4*(11), November 1999.

24. Lamb, H. (1917). On waves in an elastic plate, *Proceedings of the Royal Society of London, Series A,* Vol. 93, 1917, pp. 114.

25. Viktorov, I.A. (1967). *Rayleigh and Lamb waves – Physical Theory and Applications*. Plenum Press, NY, 1967.

26. Deutsch, W.A.K, Cheng, A. and Achenbach, J.D. (1999). Focusing of Rayleigh waves: simulation and experiment. *IEEE Transactions of Ultrasonics, Ferroelectrics, and Frequency Control, 46*(*2*), March 1999, pp. 333–340.

27. Giurgiutiu, V., Zagrai, A.N. and Bao, J. (2002) Piezoelectric wafer embedded active sensors for aging aircraft structural health monitoring. *Structural Health Monitoring – An International Journal*, Sage Pub., *1*(*1*), July 2002, pp. 41–61.